ACS APPLIED MATERIALS & INTERFACES

www.acsami.org

Research Article

"Three-in-one" Zr-MOF Multifunctional Carrier-mediated Fluorescent and Colorimetric Dual-signal Readout Biosensing Platform to Enhance Analytical Performance

Liangqiong Ren, Feng Hong, Lingwen Zeng, and Yiping Chen*

Cite This: https://doi.org/10.1021/acsami.2c16267

Read Online

ACCESS | Metrics & More | Article Recommendations | Supporting Information

ABSTRACT: To address the urgent demand for sensitive and stable detection applications, significant efforts have been made in the development of dual-signal readout assays for precise target detection and timely health risk control. Here, a new nanomaterial, Pt@PCN-224-HRP-initiator DNA (PP-HRP-iDNA), was exploited to construct a dual-signal readout biosensing platform. Zr-MOF (PCN-224) was loaded with as many Pt nanoparticles (NPs) and as much horseradish peroxidase (HRP) as possible to enhance the brightness of the colorimetric signal recognizable to the naked eye while also acting as a gatekeeper to protect the enzyme activity and ensuring the stability of the assay process. Moreover, the Pt NPs and HRP displayed a synergistic catalytic effect, which promoted the sensitivity of detection. Further, the formation of the Zr−*O*−P bond eliminated the instability of the interactions between PCN-224 and iDNA in a controllable manner. After the immunoreaction, iDNA stimulated a hybridization chain reaction, resulting in a significant reduction of the fluorescent DNA in the supernatant and a fluorescent signal change. Subsequently, the PP-HRP-iDNA probe implemented UV-light response (450 nm) where 3,3′,5,5′-tetramethylbenzidine was used as a substrate for the colorimetric signal readout. By virtue of the nanomaterial-modulated transduction mechanism and the antigen−antibody interactions, this dual-signal biosensor displays high sensitivity, with a limit of detection of 0.65 pg/mL for aflatoxin B_1 and 4 CFU/mL for *Salmonella enteritidis*, suggesting the detection potential of the biosensing platform for analyzing various targets.

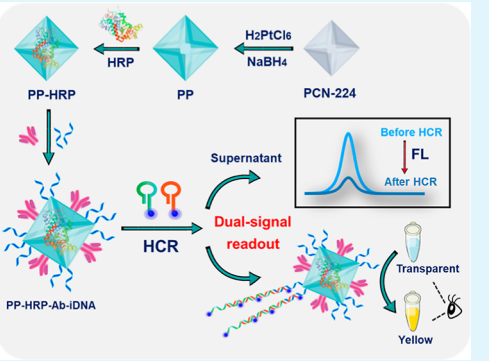

KEYWORDS: *multifunctional nanomaterials, dual-signal readout, synergistic effect, signal amplification, food safety*

INTRODUCTION

Food safety and environmental monitoring have attracted global attention due to a large variety of hazard factors,[1,2] such as foodborne pathogens,[3] mycotoxins,[4] pesticide residues,[5] heavy metals,[6] and so forth. Current approaches toward the detection of hazard factors rely on a single-signal readout mode[7,8] and face multifaceted challenges,[9] such as one component-based trace target recognition and signal transduction in a complex food matrix, which are inimical to the reliable and efficient detection of real samples. With the burgeoning advances in detection technology, the dual-signal readout mode is increasingly favored by researchers for its notable accuracy, arising from the self-calibration function.[10−13] Among these advances, colorimetric signal readouts enable semiqualitative analysis with naked-eye detection to facilitate on-site practicability.[14−17] However, their poor detection sensitivity limits their wide application.[18] Fluorescence detection techniques have appealed to researchers because of their superior performance (high sensitivity, rapid response, and stable reproducibility).[19−22] Therefore, integrating these two signal readout modes could lead to functional complementarity, enhance detection accuracy and functional versatility, and expand the range of applications. These factors are essential for the development of highly accurate, sensitive, and versatile dual-signal readout biosensing platforms to address food safety and environmental issues and guard human health against different risk factors.[23]

In recent years, Zhou et al. developed a sensitive dual-channel detection strategy using probes constructed from pomegranate-shaped dendritic silica nanospheres.[24] They employed the highly accessible mesoporous channel of the prepared probe to encapsulate a considerable number of fluorescent probes (quantum dots) and utilized the large surface area to load horseradish peroxidase-labeled antibody (HRP-Ab) for signal amplification. Despite their significant achievements in terms of the fast analysis and excellent sensitivity of this two-channel detection method, the signal amplification performance was restricted by using only the

Received: September 9, 2022
Accepted: October 21, 2022

Scheme 1. Brief Schematic Representation of the Preparation of PP-HRP-Ab-iDNA and an Ultrasensitive and Dual-Signal Readout Biosensing Platform Constructed Using the Prepared Probes

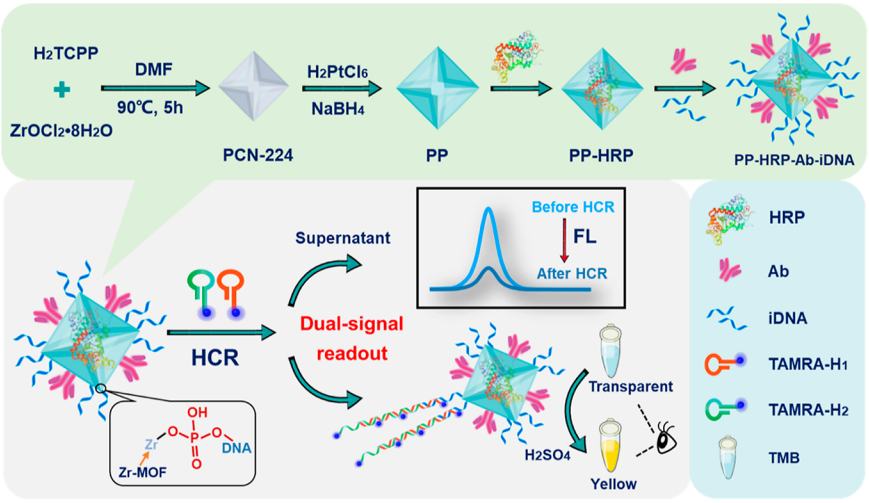

mesoporous properties and large surface area of the nanospheres to separately enrich different signal probes. The limited sensitivity posed a notable challenge in the face of detecting hazard factors with varying sensitivity requirements. Additionally, the conjugation of nanomaterials for molecular recognition involved additional coupling reagents that increased operational difficulties and may reduce the activity of the signal probe.[25−27] Thus, constructing an optimal multifunctional signal probe for the development of a fluorescent and colorimetric dual-signal readout biosensing platform with high sensitivity, accuracy, and stability is imperative.

Metal−organic frameworks (MOFs) are a prototypical case where their high porosity and large surface areas lead to an innovative direction for constructing ideal dual-signal readout probes.[28,29] Many reports have proved that MOFs can be applied as carriers for the in-situ growth of noble metals to improve detection sensitivity[30−33] and that their porosity can be utilized to encapsulate enzymes with high loadings; this has been proposed in biosensing strategies with a wide range of applications in food safety, environmental monitoring, medical diagnosis, and so forth. However, studies have neglected the application of the characteristics of the MOFs (e.g., Zr-MOF) itself. Thus, investigating how to harness the advantages of the physical structure and ligand ions of MOFs to form "smart multifunctional probes" and maintain the harmony of their various components could open up new opportunities to considerably enhance the performance of dual-signal mode biosensors.

Herein, we present a versatile biosensing platform based on a multifunctional nanomaterial probe (Scheme 1). The internal pores and external surfaces of the Zr-MOF were utilized separately for functionalization. PCN-224 was rendered as a carrier to support the growth of Pt NPs to obtain Pt@PCN-224 (PP). Subsequently, HRP was encapsulated in the internal pores of PCN-224 (forming PP-HRP) to enhance the synergy with the Pt NPs and boost the sensitivity of colorimetric detection (Scheme 1). The phosphate backbone of DNA can form Zr−*O*−P bonds with the external metal nodes of PCN-224,[34,35] a coordination chemistry strategy for the surface functionalization of the Zr-MOF with oligonucleotides, eliminating the complex manipulation and instability of the conjugated DNA. To improve the sensitivity of fluorescence detection, a hybridization chain reaction (HCR), introduced by the PCN-224-enriched initiator DNA (iDNA), was used as a signal readout and an amplification component in the fluorescence detection (Scheme 1).[36−38] After the immunoreaction, different amounts of the PP-HRP-iDNA probe were immobilized on the plates, which could, on the one hand, trigger a HCR and induce significant changes in the content of fluorescent hairpin DNA (TAMRA-H_1 and TAMRA-H_2) in the supernatant and, on the other hand, be used for color development to achieve fluorescent and colorimetric dual-signal readouts. In addition, aflatoxin B_1 (AFB_1, small molecules) and *Salmonella enteritidis* (*S. enteritidis*, macromolecules) were employed as typical analytes to validate the proposed biosensing platform. The results demonstrate that the sensitivity of both fluorescent and colorimetric detection is greatly improved by different signal amplification systems. Further, the designed signal probe not only overcomes the drawbacks of the conventional coupling problem between nanomaterials and biomolecules (Ab or DNA) but also possesses multifunctional applications. The dual-signal readout mode presents complementarity merits and improves the analytical accuracy and practical applications of biosensors. This study provides a new avenue in the application of nanomaterials to improve the analytical performance of biosensing platforms.

RESULTS AND DISCUSSION

Characterizations of the PP-HRP-Ab-iDNA Probe. The successful synthesis of the PP-HRP-Ab-iDNA probe was verified with different characterization methods, such as X-ray diffraction (XRD), scanning electron microscopy (SEM), transmission electron microscopy (TEM), energy-dispersive spectroscopy (EDS), and dynamic light scattering (DLS). The XRD pattern in Figure S1A shows the appearance of typical characteristic peaks of PCN-224. Further, some peaks appear in the high-angle region with 2θ values from 30 to 70° related to the [111], [200], and [220] planes of Pt nanoparticles (NPs). These results indicate that along with their formation, the Pt NPs were successfully loaded onto PCN-224 and that their incorporation did not significantly change the morphology of the latter. The particle sizes and morphologies were confirmed by SEM and TEM. The obtained PCN-224 grew

https://doi.org/10.1021/acsami.2c16267
ACS Appl. Mater. Interfaces XXXX, XXX, XXX−XXX

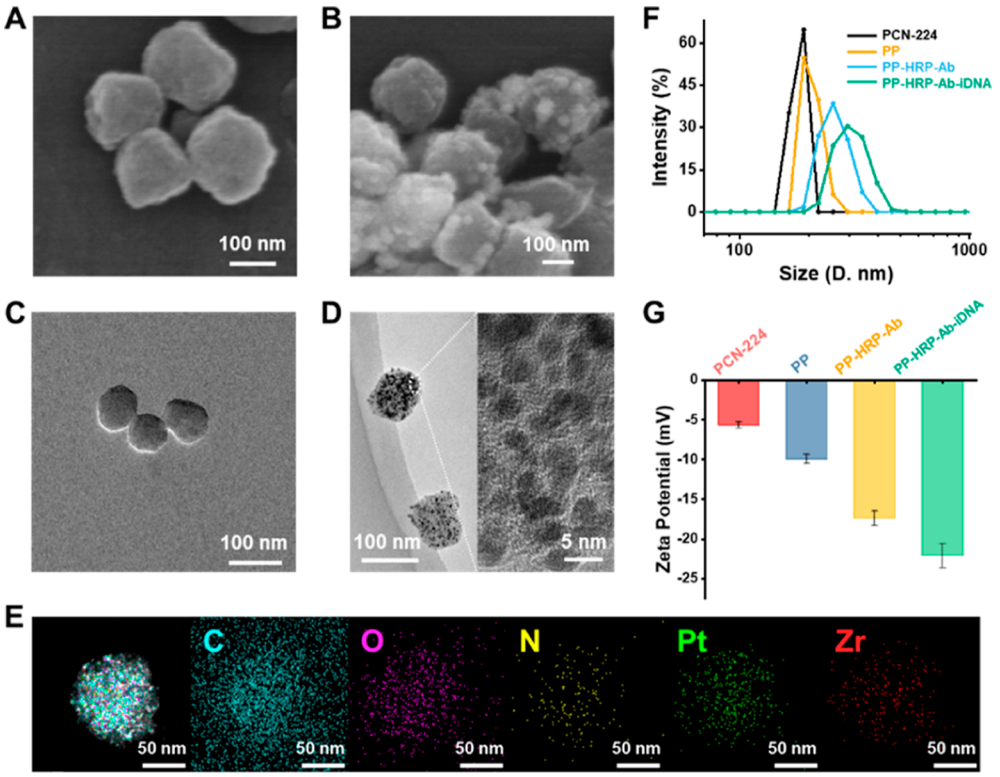

Figure 1. Characterization of functionalized PCN-224-based nanoparticles: SEM images of (A) PCN-224 and (B) PP; TEM images of (C) PCN-224 and (D) PP and enlarged Pt NPs loaded onto PCN-224; (E) corresponding TEM elemental mapping images of the elements C, O, N, Pt, and Zr; (F) hydrodynamic size changes and (G) zeta potentials of PCN-224, PP, PP-HRP-Ab, and PP-HRP-Ab-iDNA.

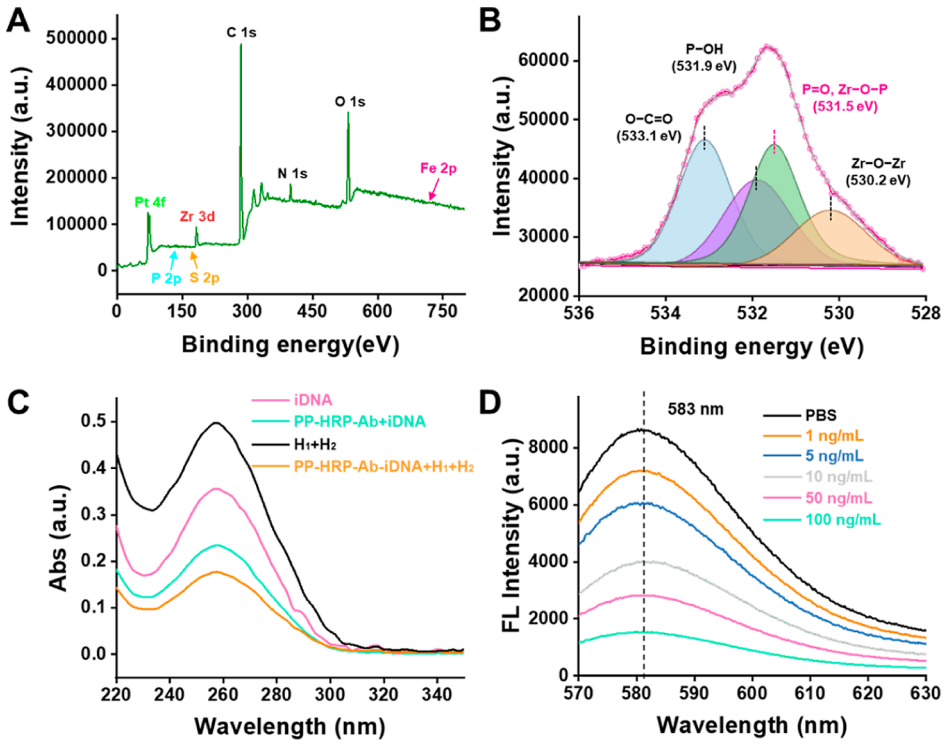

Figure 2. (A) Survey XPS spectrum and (B) O 1s XPS spectra of PP-HRP-Ab-iDNA. (C) Absorbance at 260 nm demonstrating how iDNA can bond to the MOF and the HCR reaction that occurs. (D) Fluorescence spectra of PP-HRP-Ab-iDNA probes with different concentrations.

into well-formed spherical crystals, which showed a size distribution in the region of 110 nm (Figure 1A,C). Evidently, the Pt NPs loaded onto PCN-224 were relatively uniform in size distribution (Figure 1B,D). Additionally, the elemental mapping images suggest that the elements C, O, N, Pt, and Zr were uniformly distributed on the PP, reconfirming the

https://doi.org/10.1021/acsami.2c16267
ACS Appl. Mater. Interfaces XXXX, XXX, XXX−XXX

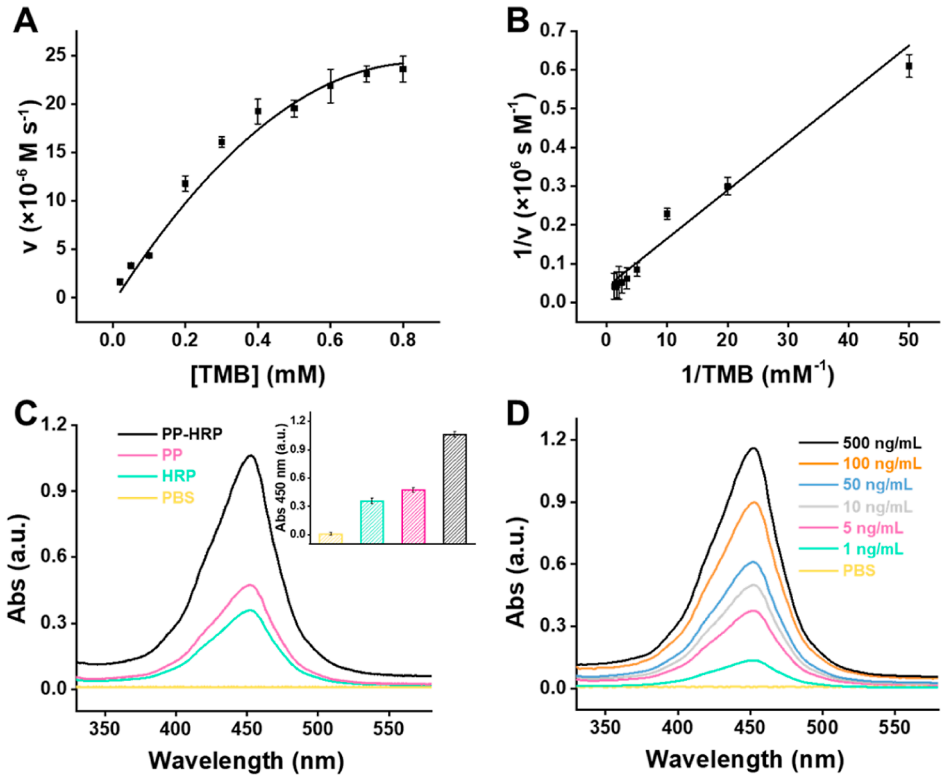

Figure 3. (A) Steady-state kinetic assay of PP-HRP as the catalyst. Plots of the initial reaction velocity for PP-HRP against TMB concentration (H_2O_2 concentration was 2.0 M); (B) double-reciprocal plots. (C) Absorbance of different enzymes. Inset: histograms comparing OD_{450} values of PBS, HRP, PP, and PP-HRP. (D) Absorbance changes of TMB with incremental increases in the concentration of the PP-HRP-Ab-iDNA probe. The error bars indicate the standard deviations of three independent measurements.

effective loading of Pt NPs onto PCN-224 (Figure 1E). Subsequently, the elemental compositions of PP-HRP-Ab-iDNA were analyzed via EDS-SEM, and the presence of N, P, S, Pt, and Zr indicates that the Pt NPs, HRP, Ab, and iDNA were successfully conjugated with PCN-224 (Figure S1B). DLS was employed to characterize the different conjugates. According to the size distribution results, the sizes of PCN-224, PP, PP-HRP-Ab, and PP-HRP-Ab-iDNA are 192.2, 200.6, 255.7, and 295.0 nm, respectively (Figure 1F). The gradual increase in the sizes of the nanomaterials suggests that the Pt NPs, HRP, Ab, and iDNA were successfully conjugated onto the surface of PCN-224. In addition, the zeta potentials of the PCN-224, PP, PP-HRP-Ab, and PP-HRP-Ab-iDNA conjugates gradually changed from −5.6 to −22.1 mV (Figure 1G). Overall, the different characterization methods revealed the successful loading of Pt NPs onto the PCN-224 unit, the incorporation of HRP into the PCN-224 aperture, the physical adsorption of Ab onto the surface of the Pt NPs, and the bonding of iDNA to the Zr ions of PCN-224.

Sensing Principle and Feasibility of PP-HRP-Ab-iDNA-Based Biosensor. In view of the abovementioned characteristics, the prepared PP-HRP-Ab-iDNA probe is capable of ultrasensitive and dual-signal detection (Scheme 1). The amount of nanomaterial probe bound to the plates could be varied according to the amount of the target based on the specific antigen−antibody immunoreaction. After binding the synthetic probe to the plates, HCRs were specifically triggered by the binding of the iDNA to the nanomaterial probe; these successive hybridization reactions bound TAMRA-H_1 and TAMRA-H_2 to the surface of the PP-HRP-Ab-iDNA probe, reducing the content of fluorescent molecules in the supernatant and affecting the fluorescent signal. However, when the fixed probe was absent, the supernatant maintained its fluorescence intensity. This enabled the quantitative analysis of the fluorescence between the target and the fluorescent signal. Regarding the colorimetric analysis, increasing the amount of the nanomaterial probe attached to the plates strengthened the catalysis of the 3,3′,5,5′-tetramethylbenzidine (TMB) oxidation reaction. The colorimetric signal reached its minimum at 450 nm when the nanomaterial probe failed to adhere to the plates. Further, a colorimetric detection method using UV−vis spectroscopy could be established. Thus, considering both the changed signals, a PP-HRP-Ab-iDNA-based dual-signal biosensor for the ultrasensitive detection of the target was developed in accordance with the integration of fluorescent and colorimetric techniques.

DNA, while exhibiting a characteristic UV−vis absorption peak at 260 nm, can form Zr−*O*−P bonds between its phosphate backbone and the Zr ions in PCN-224. First, we investigated the interaction between PP-HRP-Ab and iDNA using X-ray photoelectron spectroscopy (XPS). A variety of elements (Zr, Pt, Fe, S, P, O, N, and C) were discovered in the XPS survey spectrum of PP-HRP-Ab-iDNA. Fe and P elements came from HRP and iDNA, respectively (Figure 2A). The O 1s core-level spectrum could be analyzed as four peaks (533.1, 531.9, 531.5, and 530.2 eV) by curve-fitting, of which 531.5 eV was the peak of the formed Zr−*O*−P bond (Figure 2B). These results indicate that PP can indeed load HRP and that iDNA can interact with PP-HRP-Ab through the formation of coordinate bonds. Second, the obtained supernatants through centrifugation before and after the reaction were exposed to

https://doi.org/10.1021/acsami.2c16267
ACS Appl. Mater. Interfaces XXXX, XXX, XXX−XXX

UV−vis radiation to verify the ability of PP-HRP-Ab to interact with DNA. After the incubation of PP-HRP-Ab with iDNA and the incubation of PP-HRP-Ab-iDNA with hairpin DNA (H_1 and H_2), the intensity of the absorbance peak of the supernatant at 260 nm changed, indicating that iDNA could be assembled with PP-HRP-Ab for the first signal amplification and that PP-HRP-Ab-iDNA can trigger the HCR event to cause a hairpin DNA decrease in the supernatant for the second signal amplification (Figure 2C). Third, the quantitative performance, based on PP-HRP-Ab-mediated dual signal amplification strategy, was confirmed by incubating the concentration gradient probe with TAMRA-H_1 and TAMRA-H_2 (Figure 2D). In the absence of the probe, the fluorescent signal of the supernatant is the strongest at 583 nm under the emission wavelength of 557 nm light. As the probe concentration increases (from 0 to 100 ng/mL), the fluorescent signal of the supernatant becomes weaker using the emission peak at 583 nm as a detection signal. Therefore, the fluorescence value can be modulated by changing the amount of the PP-HRP-Ab-iDNA probe to develop the sensor.

Meanwhile, the constructed probe is activated in the presence of TMB, in which the Pt NPs and HRP can decompose H_2O_2 to generate hydroxyl radicals (•OH), leading to a color change in the substrate (from colorless to blue). The reaction is terminated by H_2SO_4, and the substrate changes from blue to yellow. The characteristic absorbance of the yellow substance occurs at 450 nm, which can reflect the catalytic activity of peroxidases. To evaluate the catalytic performance of the PCN-224 conjugate after immobilizing the Pt NPs and loading HRP, different nanomaterial probes were employed for the verification experiments. First, the catalytic efficiencies of the Pt NPs, PP, PP-HRP, and HRP were evaluated by comparing their apparent steady-state kinetic parameters. The double-reciprocal curves of PP-HRP (Figure 3B) and PP (Figure S2B) were plotted by constructing Michaelis−Menten equations to describe the relationship between the initial reaction velocities and the varying TMB concentrations (Figures 3A and S2A). Furthermore, the kinetic parameters were derived. In contrast, the kinetic parameters of HRP and Pt NPs were also listed (Table 1). Notably, the K_{cat} value of PP-HRP toward TMB was as high as 5.6×10^7 s^{-1}, which is almost 1.9-, 57.7-, and 14,000-fold greater than those of PP, Pt NPs, and HRP, respectively. The affinity of PP-HRP for TMB appeared to have a negligible change following Pt NPs and HRP loading, as evidenced by the fact that their K_m value was not significantly different. Second, along with the addition of TMB, the PBS solution did not undergo a color change. Not only was the absorbance signal of the oxidation of TMB catalyzed by PP-HRP stronger than those of the PP and HRP solutions (Figure 3C), the catalytic activity of PP-HRP was higher than the sum of the catalytic activities of PP and HRP under the same conditions (Figure 3C inset). We speculated that the synergistic effects between the Pt NPs and the enzymes played a crucial role in boosting the catalytic activity of PP-HRP. Furthermore, the HRP fixation efficiency was evaluated by coomassie blue staining with the calculated efficiency value of 3.73% (37.29 μg HRP per 1 mg of PP, Figure S3). The exceptional HRP fixation efficiency also verified that PP indeed has the ability to enrich enzymes for signal amplification. In addition, to evaluate the catalytic quantitative performance of the PP-HRP-Ab-iDNA probe, different concentrations of the prepared probe were used to catalyze the oxidation of the substrate. As the probe concentration was incremented, the colorimetric signal of the system gradually increased (Figure 3D). As expected, the PP-HRP-Ab-iDNA probe suggests an enhancement in the colorimetric signal compared to HRP, which could potentially act as a signal transformation and amplification technique in detection. For the nanomaterial probe-based ELISA, the PP-HRP-Ab-iDNA probe can be considered a labeling enzyme with wide applicability. Regarding the stability of the PP-HRP probe, negligible changes in the catalytic efficiency, morphology, and structure of PP-HRP were observed compared to HRP (vulnerability to environmental effects and easy inactivation) and PP (accessible aggregation and decreased activity) after a period of storage (Figure S4A,B).

Table 1. Comparison of the Kinetic Parameters of Various Catalysts Toward the Oxidation of TMB by H_2O_2[a]

catalyst	[E] (μM)	substrate	K_m (mM)	V_{max} (μM s^{-1})	K_{cat} (s^{-1})
Pt NPs[39]	8.2×10^{-7}	TMB	0.8	0.8	9.7×10^5
PP	5.3×10^{-7}	TMB	0.1	15.7	3.0×10^7
PP-HRP	4.4×10^{-7}	TMB	0.3	24.5	5.6×10^7
HRP[40]	2.5×10^{-5}	TMB	0.4	0.1	4.0×10^3

[a][E] represents the catalyst concentration, K_m is the Michaelis constant, V_{max} is the maximal reaction velocity, and K_{cat} is the catalytic constant that equals $V_{max}/[E]$.

Quantitative Detection of a Target Using the Proposed Dual-Signal Fluorescent and Colorimetric Sensor. Prior to the exploitation of the PP-HRP-Ab-iDNA-based colorimetric and fluorescent biosensor for quantitative analysis of the target (AFB_1 and *S. enteritidis*), the detection conditions, including the concentration and incubation time of the PP-HRP-Ab-iDNA probes, the concentrations of TAMRA-H_1 and TAMRA-H_2, and the HCR reaction time, were optimized (Figures S5 and S6). We selected the following experimental conditions to detect AFB_1: 1 μg/mL of the PP-HRP-GM-Ab-iDNA probe (GM-Ab = goat anti-mouse Ig G), 30 nmol/L of TAMRA-H_1 and TAMRA-H_2, an HCR reaction time of 50 min, and an incubation time of 30 min (Figure S5A−D). In the case of *S. enteritidis*, the optimal experimental conditions were 500 ng/mL of the PP-HRP-Ab_2-iDNA probe, 25 nmol/L of TAMRA-H_1 and TAMRA-H_2, an HCR reaction time of 50 min, and an incubation time of 30 min (Figure S6A−D).

Competitive Immunoassay of AFB_1. AFB_1, a type of mycotoxin, is a naturally occurring carcinogen and highly toxic. The rapid and highly sensitive detection of AFB_1 in food and environment is important to circumvent its risks. In this study, AFB_1 was analyzed using the constructed dual-signal fluorescent and colorimetric sensor combined with the antigen−antibody interactions. In the competitive immunoassay, different amounts of PP-HRP-GM-Ab-iDNA were bound to polystyrene 96-well plates after the specific immunoreaction, which triggered the HCR and the TMB colorimetric reaction for the signal readout. In the fluorescent quantitative analysis method, the unbound TAMRA-H_1 and TAMRA-H_2 in the supernatant were used as signal probes in the detection of fluorescence intensity. A good linear relationship between the logarithm of the AFB_1 concentration (X) and the difference in fluorescence intensity at 583 nm, ΔFL (Y), was obtained from 1 pg/mL to 100 ng/mL. The linear equation is $Y = 994.59X + 408.44$ ($X = Lg[AFB_1$ (pg/

https://doi.org/10.1021/acsami.2c16267
ACS Appl. Mater. Interfaces XXXX, XXX, XXX−XXX

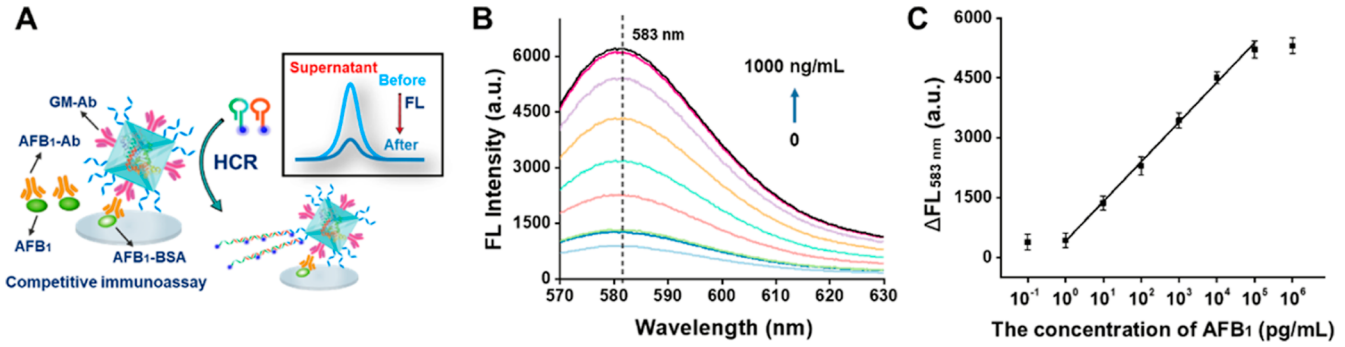

Figure 4. Fluorescence quantification of AFB_1 using the dual-signal readout biosensing platform. (A) Schematic of the competitive immunoassay for AFB_1 fluorescence detection. (B) Fluorescence spectra. (C) $\Delta FL_{583\ nm}$ with the different concentrations of AFB_1 (10^{-1}–10^6 pg/mL). The error bars indicate the standard deviations of three independent measurements.

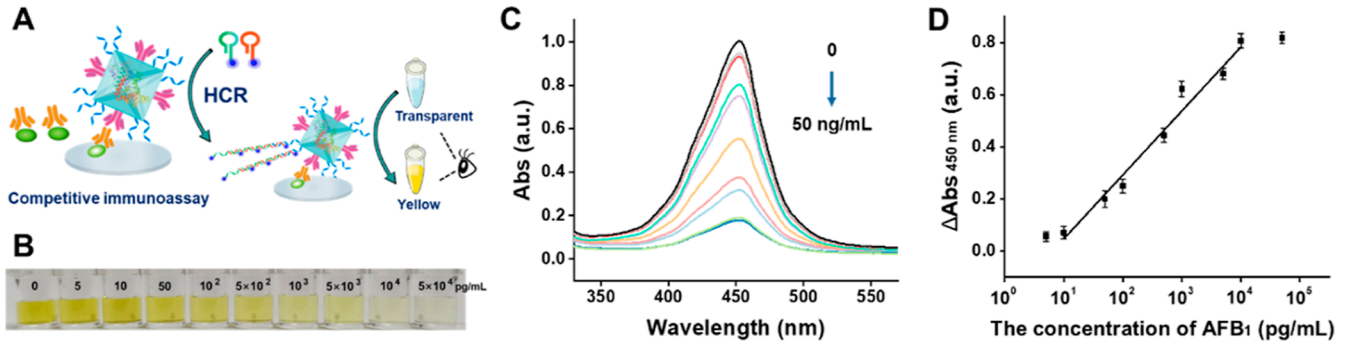

Figure 5. Colorimetric quantification of AFB_1 using the dual-signal readout biosensing platform. (A) Schematic of the competitive immunoassay for AFB_1 colorimetric detection. (B) Photograph obtained from aqueous suspensions, (C) UV–vis spectra, (D) $\Delta Abs_{450\ nm}$ with different concentrations of AFB_1 (5–5 × 10^4 pg/mL). The error bars indicate the standard deviations of three independent measurements.

mL)]) with R^2 value of 0.997 (FL_0 and FL are the mean values of the fluorescence intensity of TAMRA-labeled hairpin DNA in the absence and presence of the target, respectively, and $\Delta FL = |FL - FL_0|$). The limit of detection (LOD) is 0.65 pg/mL (LOD = 3*S*/*M*, *S* represents the value of the blank sample's standard deviation, and *M* is the slope of the calibration plot within the low concentration levels. *S* = 112.043, *M* = 514.19) (Figure 4). In the colorimetric method, the signal readout was determined by the color change in the TMB oxidation reaction catalyzed by a probe immobilized on an ELISA plate (Figure 5A). A concentration-dependent response was shown in the decreasing trend in the change in absorbance, ΔAbs, at 450 nm with increasing AFB_1 concentration (5 pg/mL–50 ng/mL; Figure 5B,C). Equally, Abs_0 (without the target) and Abs (with the target) are the median absorbance values of the reaction system, and $\Delta Abs = |Abs - Abs_0|$. The experiment showed a linear range of detection from 10 pg/mL to 10 ng/mL, and the linear equation is $Y = 0.2418X - 0.1997$ (X = Lg[AFB_1 (ng/mL)], $R^2 = 0.991$; Figure 5D). The LOD for AFB_1 detection is 3.5 pg/mL (*S* = 0.0214, *M* = 0.0183). Comparatively, the linear range of a conventional ELISA for AFB_1 detection is from 100 pg/mL to 10 ng/mL, with a linear equation of $Y = 0.2426X + 0.4392$ ($R^2 = 0.993$) and an LOD of 100 pg/mL (Figure S7). These results indicate that the LODs of the proposed fluorescent and colorimetric dual-signal method are approximately 154- and 29-fold lower, respectively, than that of the conventional HRP-ELISA method for AFB_1 detection. The HRP-ELISA method is constructed based on an antigen–antibody reaction to change the amount of HRP. However, HRP is easily inactivated, which affects the stability of the assay results. By encapsulating the enzyme into the pores of PCN-224, HRP's conformation was protected, to a certain extent, from destruction, and detection stability was ensured. The desirable porous structure and large surface area of PCN-224 allowed exposing the binding sites to the highest degree possible when loading the HRP and facilitated the accessibility of the target to the binding sites. Moreover, HRP could work synergistically with Pt NPs immobilized on PCN-224 to amplify signals and improve the detection sensitivity. Compared with other reported methods for AFB_1 detection, the sensor demonstrated better sensitivity (Table S1).

PP-HRP-GM-Ab-iDNA incubated with interferences including AFB_2, AFG_1, and AFG_2 was further used to investigate specific recognition of AFB_1 by the designed biosensor. We demonstrated that the fluorescence intensities obtained from potential interferences were much lower than that of AFB_1, indicating the high recognition specificity of the fluorescent biosensor for AFB_1 over other coexisting species (Figure S8). Contrary to these fluorescence changes, these interferences afforded apparent color transitions (from colorless to yellow) through naked eye observations, whereas the AFB_1 output remained negligible, suggesting the colorimetric sensor's visual identification capability for AFB_1. Therefore, the proposed dual-mode biosensor exhibited excellent performance in discriminating between AFB_1 and the interferences.

To confirm the feasibility of this approach using food matrices, recovery rate experiments were first conducted by spiking rice samples with different concentrations of standard AFB_1 samples. As summarized in Table S2, the AFB_1 levels determined from the fluorescent and colorimetric detection pathways were similar, supporting the accuracy of the assay. The recoveries of all assays ranged from 80.05 to 111.32%,

https://doi.org/10.1021/acsami.2c16267
ACS Appl. Mater. Interfaces XXXX, XXX, XXX–XXX

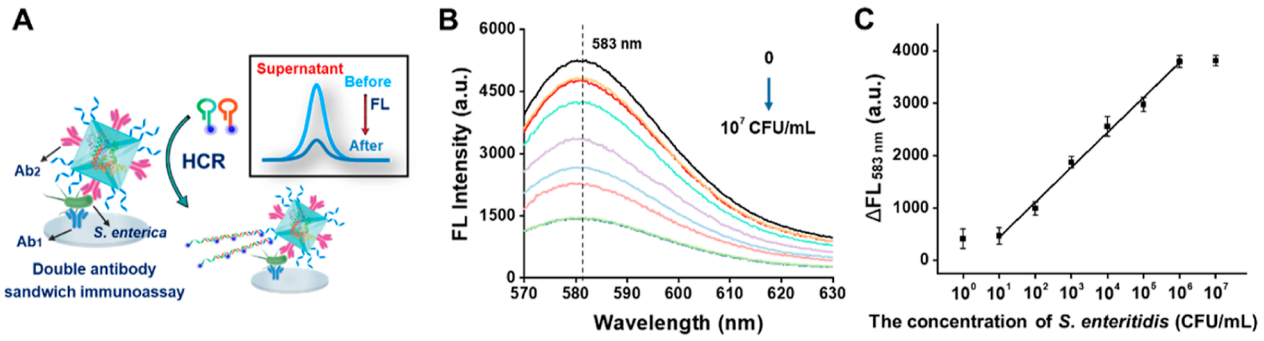

Figure 6. Fluorescence quantification of *S. enteritidis* using the double-antibody sandwich immunoassay. (A) Brief schematic representation, (B) fluorescence spectra, and (C) $\Delta FL_{583\ nm}$ with the different concentrations of *S. enteritidis* (10−10^7 CFU/mL). The error bars indicate the standard deviations of three independent measurements.

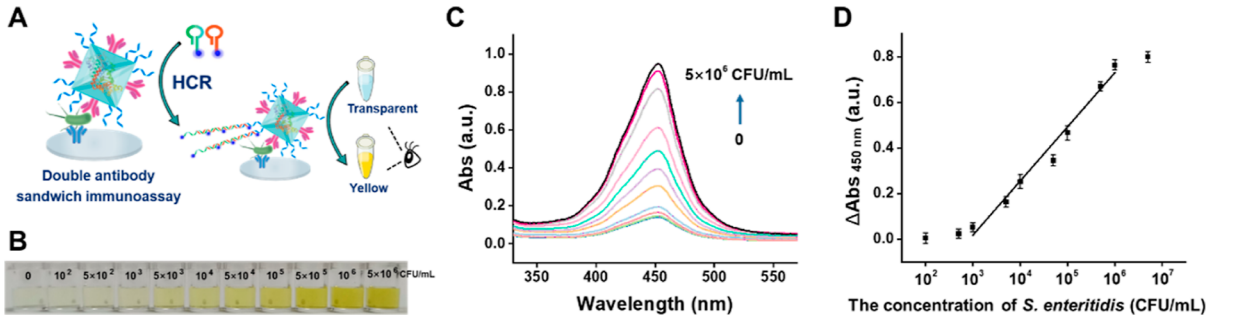

Figure 7. Colorimetric quantification of *S. enteritidis* using double-antibody sandwich immunoassay. (A) Brief schematic representation, (B) photograph obtained from aqueous suspensions, (C) UV−vis spectra, and (D) $\Delta Abs_{450\ nm}$ with the different concentrations of *S. enteritidis* (10^2−5 × 10^6 CFU/mL). The error bars indicate the standard deviations of three independent measurements.

with the coefficients of variation (CVs) ranging from 6.65 to 12.36%. This confirms the high accuracy and reliability of the proposed dual-mode probe in detecting AFB_1. In addition, some blind samples were tested using this approach and the HPLC method; the assay results showed that this approach is consistent with HPLC analysis to a good extent (Figure S9). A biosensing strategy that has ultrasensitive dual readouts ensures robust responses to trace changes in AFB_1 concentration, allowing for the precise discrimination of positive and negative results and, thus, undoubtedly boosting the reliability of bioassays.

Double-Antibody Sandwich Immunoassay of *S. enteritidis*. This biosensor was employed to detect *S. enteritidis*, a type of foodborne pathogen, which not only contaminates foods and water but also easily causes food poisoning incidents in the population. In this assay, the formation of a double-antibody sandwich immune complex among Ab_1, *S. enteritidis*, and PP-HRP-Ab_2-iDNA was the basis for the quantitative analysis of the relationship between the target and the dual-mode signals. Samples in the absence of bacteria failed to induce the binding of the probes to the plates. Therefore, the amount of unreacted TAMRA-H_1 and TAMRA-H_2 in the supernatant remained constant, resulting in a strong fluorescent signal (Figure 6A). Moreover, the TMB oxidation reaction could not be catalyzed, and the UV−vis absorption of the system was minimal (Figure 7A). The fluorescence signal intensity decreased (Figure 6B) while the colorimetric signal increased (Figure 7B,C) with the increasing amount of target. One can observe a positive relationship between ΔFL and the concentration of *S. enteritidis* (Figure 6C). Further, the linear range is from 10^1 to 10^6 CFU/mL, with a linear equation of $Y = 667.04X - 895.44$ (X = Lg[*S. enteritidis* (CFU/mL)], R^2 = 0.993). The LOD, calculated as $3S/M$, is 4 CFU/mL (S = 68.404, M = 51.594). Additionally, in the range from 10^3 to 10^6 CFU/mL, a linear relationship was obtained between ΔAbs at 450 nm (Y) and the logarithm of the *S. enteritidis* concentration (Lg[*S. enteritidis* (CFU/mL)]) as $Y = 0.2383$ Lg[*S. enteritidis* (CFU/mL)] - 0.6891 (R^2 = 0.992), while the LOD was obtained as 217 CFU/mL ($3S$ = 0.0289, M = 0.0004; Figure 7D). Furthermore, the results are indicative of a dual-signal readout assay exhibiting a more optimal performance for *S. enteritidis* detection than a previously developed method (Table S3).

The specificity of PP-HRP-Ab_2-iDNA for *S. enteritidis* in the presence of other interfering bacteria was also investigated. *S. enteritidis* triggered noticeable changes in both fluorescence intensities and colorimetric signals, but the signal changes due to other bacteria species were barely different from those of the blank sample (Figure S10). These findings demonstrated that PP-HRP-Ab_2-iDNA could act as a highly specific probe for detecting *S. enteritidis* and that the proposed biosensor resisted the interference of other bacteria. Accuracy is a key factor in appraising the practicality of a developed biosensor. Standardized milk samples spiked with *S. enteritidis* at different concentrations were investigated with the optimized biosensor. The recovery rates of *S. enteritidis* in the samples ranged from 84.36 to 108.28%, and the CVs were below 13%, showing that the dual-signal readout biosensor has acceptable specificity and reproducibility (Table S4). Meanwhile, several blind samples were analyzed using the proposed method and qPCR; the results were consistent, manifesting that the dual-signal biosensor could provide stable and ultrasensitive detection of macromolecules (*S. enteritidis*; Figure S11). The readily implemented accuracy of the assay stems from the cross-

https://doi.org/10.1021/acsami.2c16267
ACS Appl. Mater. Interfaces XXXX, XXX, XXX−XXX

checking of the dual detection results, which contributes to the detection credibility.

The above results reveal that stable, ultrasensitive, and dual-signal readouts could be readily implemented using a PP-HRP-Ab-iDNA-based biosensor. In our design, PCN-224 was the basis for the versatility of the PP-HRP-Ab-iDNA probe, serving as a support to load high-density Pt NPs and as a means to encapsulate HRP, avoiding the tedious operation of biomolecule coupling (the amino groups of Ab cross-linking with Pt NPs and the P of DNA binding to the Zr ions of PCN-224). The HCR and the synergistic effect between the Pt NPs and HRP played an important role in enhancing the probe activities, manifesting increased brightness of the colorimetric signal recognizable to the naked eye and an accurate, sensitive detection response. The results of the dual-signal response mode can be mutually verified to ensure the accuracy of the detection results, further showing the superiority of PP-HRP-Ab-iDNA.

CONCLUSIONS

In conclusion, we reported a PP-HRP-Ab-iDNA-based detection probe integrating fluorescent and colorimetric detection methods into a nanostructure, providing a simple, sensitive, and accurate route for dual-signal readout and amplification. Our results revealed that a dual-signal readout biosensing platform can conquer the limitations of current detection technologies requiring sophisticated instruments, eliminate cumbersome conjugation steps, and ensure the accuracy and simplicity of the detection process. However, there is still a deficiency in the level of automated testing. Integrating automation equipment and smartphone devices for digital signal readouts could be a useful area to explore in future research. In future studies, we anticipate developing a digital and portable assay for real-time and on-site analysis.

MATERIALS AND METHODS

Materials. Zirconyl chloride octahydrate ($ZrOCl_2{\cdot}8H_2O$), chloroplatinic acid (H_2PtCl_6), benzoic acid, and sodium borohydride ($NaBH_4$) were obtained from Aladdin Industrial Co., Ltd. Tetrakis (4-carboxyphenyl) porphyrin (H_2TCPP), N, *N*-dimethylformamide, GM-Ab, AFB_1, AFB_2, AFG_1, and AFG_2 standards were purchased from Shanghai Yuanye Bio-Technology Co., Ltd. Monoclonal mouse anti-AFB_1 (AFB_1-Ab), AFB_1 hapten (AFB_1-BSA), HRP, TMB liquid substrate, and bovine serum albumin (BSA) were purchased from Sigma (St. Louis, MO, USA). *S. enteritidis* (*S. enteritidis*, ATCC 14028), *Listeria monocytogenes* (*L. monocytogenes*, ATCC 43257), *Escherichia coli* (*E. coli*, ATCC 25922), *Staphylococcus aureus* (*S. aureus*, ATCC 29213), and *Vibrio parahaemolyticus* (*V. parahaemolyticus*, ATCC 17802) were purchased from the American Type Culture Collection (ATCC, USA). *Salmonella* monoclonal capture antibody (Ab_1) and detection antibody (Ab_2) were purchased from CalBioreagents, Inc. (San Mateo, California, USA). Other chemicals were of analytical reagent grade from Sinopharm Chemical Co., Ltd. (Shanghai, China). The water used in the experiments was deionized and ultrafiltered by the Millipore Milli-Q ion exchange device.

Oligonucleotides used in this work were purchased from and purified with a high-performance liquid chromatograph by Sangon Biological Engineering Technology & Services Co., Ltd. (Shanghai, China). The sequences were as follows (sequence 5′-3′):

Initiator DNA (iDNA): AAG TCT AGG ATT CGG CGT GGG TTA AAA AAA AAA AA-Phosphate.

TAMRA-H_1: TTA ACC CAC GCC GAA TCC TAG ACT CAA AGT AGT CTA GGA TTC GGC GTG-TAMRA.

TAMRA-H_2: TAMRA-AGT CTA GGA TTC GGC GTG GGT TAA CAC GCC GAA TCC TAG ACT ACT TTG.

Synthesis of Pt@PCN-224-HRP-Ab-iDNA. After the synthesis of Pt@PCN-224 (the detailed synthesis steps were shown in Supporting Information), HRP (1 mg/mL, 50 μL) was incubated with 1.0 mL of Pt@PCN-224 solution for 60 min. Then, Ab (100 μL, 200 μg/mL) was added to the suspension and agitated overnight. Finally, the suspension was centrifuged at 14,000 rpm (14,462 xg) for 15 min and washed three times with phosphate-buffered saline (PBS) (10 mM, pH 7.4) to obtain the ultimate PP-HRP-Ab. Then, iDNA (1 μM, 500 μL) was added at 37 °C for 30 min. Next, the mixture solution was washed with PBS three times with centrifugation [13,500 rpm (13,447 xg), 15 min], resuspended in 1.0 mL of PBS, and stored at 4 °C before use.

Detection of AFB_1. First, we modified a polystyrene 96-well plate with AFB_1-BSA (100 μL) diluted in a carbonate buffer (0.2 M sodium carbonate/bicarbonate, pH 9.6) at 4 °C overnight. After discarding the solution, the plate was washed three times with PBST (0.05% Tween-20 in 10 mM, pH = 7.4 PBS buffer) and then blocked with 3% BSA (3% BSA in PBST buffer) (200 μL) at 37 °C for 1 h to reduce the nonspecific binding. After washing in the same way, AFB_1 standard solution with varying concentrations (0, 10^{-1}, 10^0, 10^1, 10^2, 10^3, 10^4, 10^5, and 10^6 pg/mL, 50 μL) and AFB_1-Ab (50 μL) were added into the wells of the plate at 37 °C for 30 min. After washing thrice, PP-HRP-GM-Ab-iDNA (100 μL) was added and then incubated at 37 °C for 30 min, resulting in different amounts of PP-HRP-GM-Ab-iDNA in the wells.

Fluorescence detection: TAMRA-H_1 and TAMRA-H_2 (50 μL) were added to the wells and incubated at 37 °C for 1 h. Then, the supernatant was taken in a clean centrifuge tube and mixed with 200 μL of water. The fluorescence intensity of the suspension was recorded by a fluorescence spectrophotometer.

UV−vis detection: Commercial TMB (100 μL) was added to the wells and incubated for 15 min at room temperature. TMB was oxidized by PP-HRP-GM-Ab-iDNA fixed on the plates through a specific reaction. Then, the reaction system was terminated by H_2SO_4 (2 M, 50 μL) for color analysis. The spectra of the solutions by UV−vis spectrometry were collected.

Detection of *S. enteritidis*. The procedures of the double-sandwich immunoassay to detect *S. enteritidis* are as follows: Ab_1, as the coating antibody was diluted with carbonate buffer (100 μL) and incubated in polystyrene wells at 4 °C overnight. Then, the wells were washed with PBST three times. We used a 3% BSA buffer (200 μL) as a blocking buffer to block the unbinding site at 37 °C for 1 h. Excess BSA was removed by repeated washing. Subsequently, 100 μL of different concentrations of *S. enteritidis* (0, 10^0, 10^1, 10^2, 10^3, 10^4, 10^5, 10^6, and 10^7 CFU/mL) in PBS were transferred to their individual wells. After incubation at 37 °C for 30 min, the wells were washed three times with PBST buffer to remove the bacteria solution, and then Ab_2 (100 μL) was added to react at 37 °C for 30 min. Next, the complex was washed thrice. PP-HRP-Ab_2-iDNA (100 μL) was added and then incubated at 37 °C for 30 min. The supernatant was discarded, and the formed complex of each sample was washed thrice. TAMRA-H_1 and TAMRA-H_2 were mixed with the complex. The supernatant was collected to detect the fluorescence intensity via a fluorescence spectrophotometer. Subsequently, commercial TMB and H_2SO_4 were employed for color reaction. The measurement procedure was the same as above.

ASSOCIATED CONTENT

Supporting Information

The Supporting Information is available free of charge at https://pubs.acs.org/doi/10.1021/acsami.2c16267.

Materials and methods and synthetic, experimental, and calculation details; XRD patterns and EDS elemental analysis; steady-state kinetic assay of PP NPs as the catalyst; HRP fixation efficiency value; catalytic efficiency at various storage times; optimization of the

https://doi.org/10.1021/acsami.2c16267
ACS Appl. Mater. Interfaces XXXX, XXX, XXX−XXX

experimental condition for AFB_1 and *S. enteritidis* detection; AFB_1 detection using conventional HRP-ELISA approach; specificity for detecting $AFB_1$and *S. enteritidis*; detection of AFB_1 in rice samples and *S. enteritidis* in milk samples using dual signal readout sensor and other methods; comparison of different methods for AFB_1 detection; recoveries of AFB_1 from rice samples; comparison of different methods for *S. enteritidis* detection; and recoveries of *S. enteritidis* in spiked milk samples (PDF)

AUTHOR INFORMATION

Corresponding Author

Yiping Chen − *College of Food Science and Technology, Huazhong Agricultural University, Wuhan 430070, China; Guangdong Laboratory for Lingnan Modern Agriculture, Guangzhou 510642 Guangdong, China; Shenzhen Institute of Food Nutrition and Health, Huazhong Agricultural University, Wuhan 430070 Hubei, China;* orcid.org/0000-0001-9309-2730; Email: chenyiping@mail.hzau.edu.cn

Authors

Liangqiong Ren − *College of Food Science and Technology, Huazhong Agricultural University, Wuhan 430070, China; Shenzhen Institute of Food Nutrition and Health, Huazhong Agricultural University, Wuhan 430070 Hubei, China*

Feng Hong − *College of Food Science and Technology, Huazhong Agricultural University, Wuhan 430070, China*

Lingwen Zeng − *Foshan University, Foshan 528051 Guangdong, China*

Complete contact information is available at: https://pubs.acs.org/10.1021/acsami.2c16267

Author Contributions

The manuscript was written through contributions of all authors. All authors have given approval to the final version of the manuscript.

Notes

The authors declare no competing financial interest.

ACKNOWLEDGMENTS

This work was financially supported by the Laboratory of Lingnan Modern Agriculture Project (NZ2021036), the National Natural Science Foundation of China (32172293), the Wuhan Science and Technology Planning Project (2020030603012347), and the Key R&D Program of Hubei Province (2020BBA053).

REFERENCES

(1) Wang, P.; Xie, L.; Joseph, E. A.; Li, J.; Su, X.; Zhou, H. Metal-Organic Frameworks for Food Safety. *Chem. Rev.* **2019**, *119*, 10638−10690.

(2) Hao, L.; Wang, W.; Shen, X.; Wang, S.; Li, Q.; An, F.; Wu, S. A Fluorescent DNA Hydrogel Aptasensor Based on the Self-Assembly of Rolling Circle Amplification Products for Sensitive Detection of Ochratoxin A. *J. Agr. Food Chem.* **2020**, *68*, 369−375.

(3) Wu, P.; Xue, F.; Zuo, W.; Yang, J.; Liu, X.; Jiang, H.; Dai, J.; Ju, Y. A Universal Bacterial Catcher Au-PMBA-Nanocrab-Based Lateral Flow Immunoassay for Rapid Pathogens Detection. *Anal. Chem.* **2022**, *94*, 4277−4285.

(4) Li, J.; Yan, H.; Tan, X.; Lu, Z.; Han, H. Cauliflower-Inspired 3D SERS Substrate for Multiple Mycotoxins Detection. *Anal. Chem.* **2019**, *91*, 3885−3892.

(5) Yu, L.; Chang, J.; Zhuang, X.; Li, H.; Hou, T.; Li, F. Two-Dimensional Cobalt-Doped Ti_3C_2 MXene Nanozyme-Mediated Homogeneous Electrochemical Strategy for Pesticides Assay Based on In Situ Generation of Electroactive Substances. *Anal. Chem.* **2022**, *94*, 3669−3676.

(6) Venkatesan, M.; Veeramuthu, L.; Liang, F.; Chen, W.; Cho, C.; Chen, C.; Chen, J.; Yan, Y.; Chang, S.; Kuo, C. Evolution of Electrospun Nanofibers Fluorescent and Colorimetric Sensors for Environmental Toxicants, pH, Temperature, and Cancer Cells − A Review with Insights on Applications. *Chem. Eng. J.* **2020**, *397*, 125431.

(7) Li, W.; Diao, K.; Qiu, D.; Zeng, Y.; Tang, K.; Zhu, Y.; Sheng, Y.; Wen, Y.; Li, M. A highly-sensitive and selective antibody-like sensor based on molecularly imprinted poly(L-arginine) on COOH-MWCNTs for electrochemical recognition and detection of deoxynivalenol. *Food Chem.* **2021**, *350*, 129229.

(8) Akhavan-Tafti, H.; Binger, D. G.; Blackwood, J. J.; Chen, Y.; Creager, R. S.; de Silva, R.; Eickholt, R. A.; Gaibor, J. E.; Handley, R. S.; Kapsner, K. P.; Lopac, S. K.; Mazelis, M. E.; McLernon, T. L.; Mendoza, J. D.; Odegaard, B. H.; Reddy, S. G.; Salvati, M.; Schoenfelner, B. A.; Shapir, N.; Shelly, K. R.; Todtleben, J. C.; Wang, G.; Xie, W. A Homogeneous Chemiluminescent Immunoassay Method. *J. Am. Chem. Soc.* **2013**, *135*, 4191−4194.

(9) Chang, J.; Lv, W.; Li, Q.; Li, H.; Li, F. One-Step Synthesis of Methylene Blue-Encapsulated Zeolitic Imidazolate Framework for Dual-Signal Fluorescent and Homogeneous Electrochemical Biosensing. *Anal. Chem.* **2020**, *92*, 8959−8964.

(10) Chang, J.; Li, H.; Li, F. Diffusivity and intercalation of electroactive dyes-mediated truly ratiometric homogeneous electrochemical strategy for highly sensitive biosensing. *Chem. Commun.* **2019**, *55*, 10603−10606.

(11) Wang, H.; Pu, G.; Devaramani, S.; Wang, Y.; Yang, Z.; Li, L.; Ma, X.; Lu, X. Bimodal Electrochemiluminescence of G-CNQDs in the Presence of Double Coreactants for Ascorbic Acid Detection. *Anal. Chem.* **2018**, *90*, 4871−4877.

(12) Cai, X.; Zheng, B.; Zhou, Y.; Younis, M. R.; Wang, F.; Zhang, W.; Zhou, Y.; Xia, X. Synergistically mediated enhancement of cathodic and anodic electrochemiluminescence of graphene quantum dots through chemical and electrochemical reactions of coreactants. *Chem. Sci.* **2018**, *9*, 6080−6084.

(13) Zhou, Y.; Huang, X.; Hu, X.; Tong, W.; Leng, Y.; Xiong, Y. Recent advances in colorimetry/fluorimetry-based dual-modal sensing technologies. *Biosens. Bioelectron.* **2021**, *190*, 113386.

(14) Teng, Y.; Shi, J.; Pong, P. W. T. Sensitive and Specific Colorimetric Detection of Cancer Cells Based on Folate-Conjugated Gold-Iron-Oxide Composite Nanoparticles. *ACS Appl. Nano Mater.* **2019**, *2*, 7421−7431.

(15) Wang, K.; Fan, D.; Liu, Y.; Dong, S. Cascaded multiple amplification strategy for ultrasensitive detection of HIV/HCV virus DNA. *Biosens. Bioelectron.* **2017**, *87*, 116−121.

(16) Zheng, S.; Li, D.; Fodjo, E. K.; Deng, W. Colorimetric/fluorescent/SERS triple-channel sensing of Cu^{2+} in real systems based on chelation-triggered self-aggregation. *Chem. Eng. J.* **2020**, *399*, 125840.

(17) Chen, R.; Chen, X.; Zhou, Y.; Lin, T.; Leng, Y.; Huang, X.; Xiong, Y. Three-in-One″ Multifunctional Nanohybrids with Colorimetric Magnetic Catalytic Activities to Enhance Immunochromatographic Diagnosis. *ACS Nano* **2022**, *16*, 3351−3361.

(18) Zhang, Y.; Xia, J.; Zhang, F.; Wang, Z.; Liu, Q. A dual-channel homogeneous aptasensor combining colorimetric with electrochemical strategy for thrombin. *Biosens. Bioelectron.* **2018**, *120*, 15−21.

(19) Li, Y.; Li, S.; Bao, M.; Zhang, L.; Carraro, C.; Maboudian, R.; Liu, A.; Wei, W.; Zhang, Y.; Liu, S. Pd Nanoclusters Confined in ZIF-8 Matrixes for Fluorescent Detection of Glucose and Cholesterol. *ACS Appl. Nano Mater.* **2021**, *4*, 9132−9142.

(20) Chen, L.; Song, L.; Zhang, Y.; Wang, P.; Xiao, Z.; Guo, Y.; Cao, F. Nitrogen and Sulfur Codoped Reduced Graphene Oxide as a General Platform for Rapid and Sensitive Fluorescent Detection of Biological Species. *ACS Appl. Mater. Interfaces* **2016**, *8*, 11255−11261.
(21) Chen, P.; Wang, Y.; He, Y.; Huang, K.; Wang, X.; Zhou, R.; Liu, T.; Qu, R.; Zhou, J.; Peng, W.; Li, M.; Bai, Y.; Chen, J.; Huang, J.; Geng, J.; Xie, Y.; Hu, W.; Ying, B. Homogeneous Visual and Fluorescence Detection of Circulating Tumor Cells in Clinical Samples via Selective Recognition Reaction and Enzyme-Free Amplification. *ACS Nano* **2021**, *15*, 11634−11643.
(22) Li, J.; Huang, X.; Zhao, X.; Chen, L. J.; Yan, X. P. pH-Responsive Torpedo-Like Persistent Luminescence Nanoparticles for Autofluorescence-Free Biosensing and High-Level Information Encryption. *Angew. Chem., Int. Ed.* **2021**, *60*, 2398−2405.
(23) Ma, L.; Peng, L.; Yin, L.; Liu, G.; Man, S. CRISPR-Cas12a-Powered Dual-Mode Biosensor for Ultrasensitive and Cross-validating Detection of Pathogenic Bacteria. *ACS Sens* **2021**, *6*, 2920−2927.
(24) Chen, C.; Zhao, D.; Wang, B.; Ni, P.; Jiang, Y.; Zhang, C.; Yang, F.; Lu, Y.; Sun, J. Alkaline Phosphatase-Triggered in Situ Formation of Silicon-Containing Nanoparticles for a Fluorometric and Colorimetric Dual-Channel Immunoassay. *Anal. Chem.* **2020**, *92*, 4639−4646.
(25) Liu, S.; Dou, L.; Yao, X.; Zhang, W.; Zhao, B.; Wang, Z.; Ji, Y.; Sun, J.; Xu, B.; Zhang, D.; Wang, J. Polydopamine nanospheres as high-affinity signal tag towards lateral flow immunoassay for sensitive furazolidone detection. *Food Chem.* **2020**, *315*, 126310.
(26) Han, S. I.; Lee, S. W.; Cho, M. G.; Yoo, J. M.; Oh, M. H.; Jeong, B.; Kim, D.; Park, O. K.; Kim, J.; Namkoong, E.; Jo, J.; Lee, N.; Lim, C.; Soh, M.; Sung, Y. E.; Yoo, J.; Park, K.; Hyeon, T. Epitaxially Strained CeO_2 /Mn_3O_4 Nanocrystals as an Enhanced Antioxidant for Radioprotection. *Adv. Mater.* **2020**, *32*, 2001566.
(27) Dong, S.; Dong, Y.; Jia, T.; Liu, S.; Liu, J.; Yang, D.; He, F.; Gai, S.; Yang, P.; Lin, J. GSH-Depleted Nanozymes with Hyperthermia-Enhanced Dual Enzyme-Mimic Activities for Tumor Nanocatalytic Therapy. *Adv. Mater.* **2020**, *32*, 2002439.
(28) Aulakh, D.; Pyser, J. B.; Zhang, X.; Yakovenko, A. A.; Dunbar, K. R.; Wriedt, M. Metal-Organic Frameworks as Platforms for the Controlled Nanostructuring of Single-Molecule Magnets. *J. Am. Chem. Soc.* **2015**, *137*, 9254−9257.
(29) Sato, H.; Matsui, T.; Chen, Z.; Pirillo, J.; Hijikata, Y.; Aida, T. Photochemically Crushable and Regenerative Metal-Organic Framework. *J. Am. Chem. Soc.* **2020**, *142*, 14069−14073.
(30) Han, Y.; Xu, H.; Su, Y.; Xu, Z.; Wang, K.; Wang, W. Noble metal (Pt, Au@Pd) nanoparticles supported on metal organic framework (MOF-74) nanoshuttles as high-selectivity CO_2 conversion catalysts. *J. Catal.* **2019**, *370*, 70−78.
(31) Luan, Q.; Gan, N.; Cao, Y.; Li, T. Mimicking an Enzyme-Based Colorimetric Aptasensor for Antibiotic Residue Detection in Milk Combining Magnetic Loop-DNA Probes and CHA-Assisted Target Recycling Amplification. *J. Agr. Food Chem.* **2017**, *65*, 5731−5740.
(32) Shi, Y.; Liu, Z.; Liu, R.; Wu, R.; Zhang, J. DNA-encoded MXene-Pt nanozyme for enhanced colorimetric sensing of mercury ions. *Chem. Eng. J.* **2022**, *442*, 136072.
(33) Zhang, T.; Lu, N.; Wang, C.; Zhang, R.; Chen, W.; Zhang, Z.; Xing, D. Biomimetic cascade nanoreactor with triple-enzyme mimetic activities for colorimetric detection of acid phosphatase. *Chem. Eng. J.* **2022**, *437*, 135267.
(34) Wang, S.; McGuirk, C. M.; Ross, M. B.; Wang, S.; Chen, P.; Xing, H.; Liu, Y.; Mirkin, C. A. General and direct method for preparing oligonucleotide-functionalized metal-organic framework nanoparticles. *J. Am. Chem. Soc.* **2017**, *139*, 9827.
(35) Nonglaton, G.; Benitez, I. O.; Guisle, I.; Pipelier, M.; Léger, J.; Dubreuil, D.; Tellier, C.; Talham, D. R.; Bujoli, B. New Approach to Oligonucleotide Microarrays Using Zirconium Phosphonate-Modified Surfaces. *J. Am. Chem. Soc.* **2004**, *126*, 1497−1502.
(36) Hong, F.; Chen, X.; Cao, Y.; Dong, Y.; Wu, D.; Hu, F.; Gan, N. Enzyme- and label-free electrochemical aptasensor for kanamycin detection based on double stir bar-assisted toehold-mediated strand displacement reaction for dual-signal amplification. *Biosens. Bioelectron.* **2018**, *112*, 202−208.
(37) Ge, Z.; Lin, M.; Wang, P.; Pei, H.; Yan, J.; Shi, J.; Huang, Q.; He, D.; Fan, C.; Zuo, X. Hybridization Chain Reaction Amplification of MicroRNA Detection with a Tetrahedral DNA Nanostructure-Based Electrochemical Biosensor. *Anal. Chem.* **2014**, *86*, 2124−2130.
(38) Zeng, W.; Liao, N.; Lei, Y.; Zhao, J.; Chai, Y.; Yuan, R.; Zhuo, Y. Hemin as electrochemically regenerable co-reaction accelerator for construction of an ultrasensitive PTCA-based electrochemiluminescent aptasensor. *Biosens. Bioelectron.* **2018**, *100*, 490−496.
(39) Xi, Z.; Wei, K.; Wang, Q.; Kim, M. J.; Sun, S.; Fung, V.; Xia, X. Nickel−Platinum Nanoparticles as Peroxidase Mimics with a Record High Catalytic Efficiency. *J. Am. Chem. Soc.* **2021**, *143*, 2660−2664.
(40) Gao, L.; Zhuang, J.; Nie, L.; Zhang, J.; Zhang, Y.; Gu, N.; Wang, T.; Feng, J.; Yang, D.; Perrett, S.; Yan, X. Intrinsic peroxidase-like activity of ferromagnetic nanoparticles. *Nat. Nanotechnol.* **2007**, *2*, 577−583.

https://doi.org/10.1021/acsami.2c16267
ACS Appl. Mater. Interfaces XXXX, XXX, XXX−XXX